PNAS RESEARCH ARTICLE | GENETICS

TMEM161B modulates radial glial scaffolding in neocortical development

Lu Wang[a,b], Caleb Heffner[c], Keng loi Vong[a,b], Chelsea Barrows[a,b], Yoo-Jin Ha[a,d], Sangmoon Lee[a,b], Pablo Lara-Gonzalez[e], Ishani Jhamb[a,b], Dennis Van Der Meer[f], Robert Loughnan[g], Nadine Parker[f], David Sievert[a,b], Swapnil Mittal[a,b], Mahmoud Y. Issa[h], Ole A. Andreassen[f], Anders Dale[a,f,g], William B. Dobyns[i], Maha S. Zaki[h], Stephen A. Murray[c], and Joseph G. Gleeson[a,b,1]

Edited by Tamara Caspary, Emory University, Atlanta, GA; received June 14, 2022; accepted December 15, 2022 by Editorial Board Member Matthew P. Scott

***TMEM161B* encodes an evolutionarily conserved widely expressed novel 8-pass transmembrane protein of unknown function in human. Here we identify *TMEM161B* homozygous hypomorphic missense variants in our recessive polymicrogyria (PMG) cohort. Patients carrying *TMEM161B* mutations exhibit striking neocortical PMG and intellectual disability. *Tmem161b* knockout mice fail to develop midline hemispheric cleavage, whereas knock-in of patient mutations and patient-derived brain organoids show defects in apical cell polarity and radial glial scaffolding. We found that TMEM161B modulates actin filopodia, functioning upstream of the Rho-GTPase CDC42. Our data link *TMEM161B* with human PMG, likely regulating radial glia apical polarity during neocortical development.**

TMEM161B | gyrification | CDC42 | knock-in crispant mice | patient-derived brain organoids

Significance

Neocortical folding (i.e., gyrification) is a fundamental evolutionary mechanism allowing the expansion of cortical surface area and increased cognitive function. Increased gyrification has been correlated with intelligence across species but has been difficult to study molecularly in non-gyrated animal models. Here we identify a role for *TMEM161B* in human gyrification, establishing cellular polarity and structural integrity of radial glial fibers of the developing brain.

Gyrification (i.e., folding) of the mammalian cerebral cortex remains one of the most fascinating phenomena of developmental neuroscience and evolution, regulated by cellular, genetic, and mechanical determinants. Cortical folding is characterized by the alternation of bulges (gyri) and fissures (sulci) of the cortical mantle, which in the primate mature brain, display remarkable periodicity of ~1.5 cm over the entire surface (1, 2). While discrete gyral and sulcal functions remain unclear, folding allows for dramatic increase in surface area, correlated with presumed cognitive function (3).

Polymicrogyria (PMG) is one of the classical types of malformations of cortical development showing an excessive number of tightly packed folds. PMG typically shows gyri more closely spaced than 1.5 cm apart. PMG can be localized to certain lobar regions or impact the entire cortex (4), often associated with defects in cellular lamination and leptomeningeal integrity (5). Prior studies associated PMG with defects in cortical patterning (*GPR56*, and *RTTN*), cell specification (*EOMES*), DNA repair (*NHEJ1*), neuronal migration (*TUBB* family genes) or tight junctions (*OCLN*), but most cases remain without molecular cause (6).

Radial glial cells (RGCs) are a population of highly polarized progenitors giving rise to neurons and glia (7). Their uniform radial orientation provides both the source of progenitor neurons as well as a scaffolding system that bridges between the apical surface and the pial basement membrane to support the migration of daughter cells required for cortical expansion (8–10). The regulation and maintenance of this system is under control of multiple cytoskeletal factors including the Rho GTPase CDC42 pathway regulating actin at the apical surface (11, 12).

Transmembrane protein 161B (TMEM161B), and its paralog TMEM161A, are highly evolutionarily conserved 8-pass transmembrane proteins of unknown function. The TMEM161 family arose early in eukaryotes, duplicating in vertebrates. Both paralogues are expressed widely in most cell types (13, 14). A recent report indicates localization to the cell membrane of excitable cell types to regulate cardiac rhythm in fish and mouse (14). However, functions in human remain unknown.

Results

Biallelic *TMEM161B* Mutations in Human Cortical PMG. In our recessive PMG cohort, we identified four families with affected children showing nearly identical neocortical PMG (Fig. 1 *A* and *B* and Table 1). Brain imaging in each showed dramatic symmetrical PMG, without a clear lobar or regional predominance (Fig. 1*B* and *SI Appendix*, Fig. S1 *A–P*). Whole-exome sequencing of one or both affected members in each family revealed a likely pathogenic variant in *TMEM161B* (*SI Appendix*, Table S1), segregating with recessive inheritance. Families I and II showed a homozygous missense c.949C>T; p.W317R.

Author contributions: L.W. designed research; L.W., C.H., K.V., Y.-J.H., S.L., P.L.-G., D.S., and S.M. performed research; M.Y.I., M.S.Z., and S.A.M. contributed new reagents/analytic tools; L.W., C.H., K.V., C.B., Y.-J.H., S.L., P.L.-G., D.V., R.L., N.P., O.A.A., A.D., W.B.D., M.S.Z., and S.A.M. analyzed data; J.G.G. supervise the project; and L.W., I.J., D.S., and J.G.G. wrote the paper.

Competing interest statement: The authors declare a competing interest. The authors have organizational affiliations to disclose, OAA is a consultant to HealthLytix.

This article is a PNAS Direct Submission. T.C. is a guest editor invited by the Editorial Board.

[1]To whom correspondence may be addressed. Email: jogleeson@ucsd.edu.

This article contains supporting information online at https://www.pnas.org/lookup/suppl/doi:10.1073/pnas.2209983120/-/DCSupplemental.

Published January 20, 2023.

Families III and IV showed a homozygous missense c.254T>G; p.L85R. All variants occurred in residues that were fully conserved in sequenced vertebrates and occurred on blocks of homozygosity (Fig. 1 *C* and *D* and *SI Appendix*, Table S2).

By mapping the mutations onto the predicted protein structure with "Alpha Fold," we found *TMEM161B* p.L85R mutation fell in the first extracellular domain, whereas p.W317R fell within the sixth transmembrane domain, and both mutations were predicted "damaging" by MutationTaster2021 (*SI Appendix*, Fig. S1 *Q–S*) (15, 16). Lysates of primary dermal fibroblast cell lines from both affected members of Family I showed substantially reduced *TMEM161B* protein levels on western blot compared to the father (*SI Appendix*, Fig. S1 *T* and *U*). These results together suggest the loss of *TMEM161B* impacts neocortical development and folding in humans.

***TMEM161B* Mutations Disrupt Apical Tight Junctions in Early-Stage Human Brain Organoids (BOs).** Public databases indicate *TMEM161B* expression across most tissues, including brain (*SI Appendix*, Fig. S2*A*). We accessed published human fetal brain single-cell RNAseq data, and found widespread expression, including in *SOX2*$^+$ RGC, *NEUROD6*$^+$ immature neurons, *DLX1*$^+$ interneuron progenitors, and *HOPX*$^+$ outer RGC (*SI Appendix*, Fig. S2 *B–G*) (17).

We next generated iPSCs using standard methods from fibroblasts from father (obligate mutation carrier), both affected members of Family I, and a second unrelated healthy control, then derived BOs (*SI Appendix*, Fig. S2 *H–J*) (18, 19). Parent and control early day in vitro (DIV) 28 BOs showed typical neural rosettes consisting of central apical tight junctions and circumferential layers of SOX2$^+$ progenitor RGC encased by TUJ1$^+$ immature neurons (18, 20). We found obvious gross abnormalities in BOs from both patients as early DIV28, with bulbous "tags" appended to one or both sides in every BO analyzed, never observed in father or control BOs (Fig. 2*A* and *SI Appendix*, Fig. S2*K*). Sectioning patient organoids showed these tags were typically cell-sparse regions surrounded by TUJ1$^+$ fibers (Fig. 2*B*), suggesting *TMEM161B* is required for BO surface integrity.

We also found patient BOs showed dramatic disorganization of rosettes at DIV28, where the typical radially oriented polarity of SOX2$^+$ RGC's surrounding an apical lumen instead showed seemingly random polarity, without a clear apical lumen (Fig. 2 *C–H* and *SI Appendix*, Fig. S2*K*). The overall disorganization precluded a careful assessment of rosette number and density, but subjectively these appeared fewer in number, suggesting a role for *TMEM161B* in rosette organization through regulation of apical lumen formation. To test this, we stained for ZO-1, an apical tight-junction marker. We found absence of ZO-1$^+$ signals from the rosette lumen in nearly every patient BOs examined (Fig. 2 *I–K* and *SI Appendix*, Fig. S2*K*). These results suggest a defect in apical junction formation leading to defective BO surface integrity.

Late-Stage TMEM161B Mutant BOs Show Irregular Radial Glial Fiber Scaffolding. CTIP2 marks deep-layer cortical neurons and is one of the first markers of neurons generated from SOX2$^+$ progenitors (21). At DIV 52 of BOs differentiation, control organoids showed CTIP2$^+$ cells uniformly surrounded the

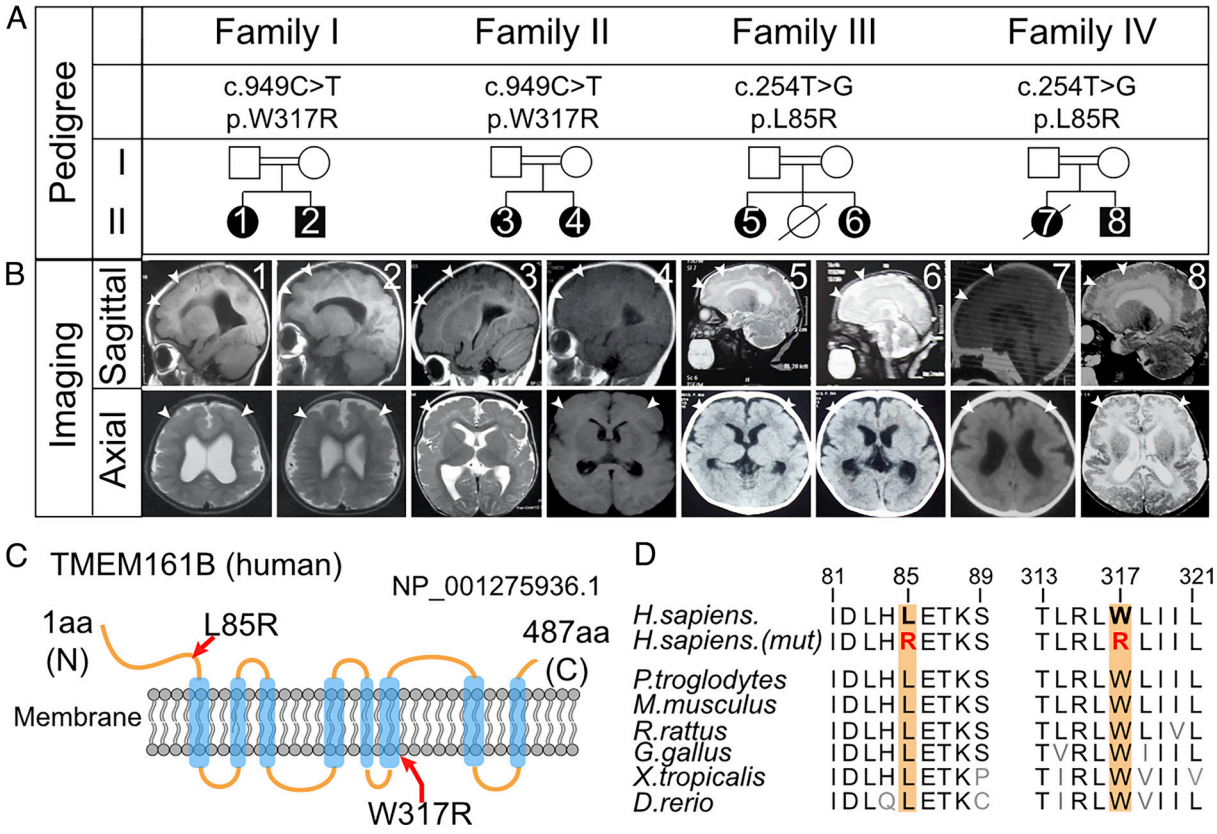

Fig. 1. Biallelic mutations in *TMEM161B* cause polymicrogyria. (*A*) Pedigrees I to IV. Double line: consanguinity. Square: male; Circle: female; filled: affected; hash line: deceased. Families I and II, as well as III and IV, share identical homozygous missense mutation c.949C>T (p.W317R) and c. 254T>G (p.L85R) respectively. (*B*) Brain imaging (midline sagittal: *Top*, axial: *Bottom*) for affected A1 to A8 showing symmetrical excessive cortical folding (arrows). (*C*) TMEM161B protein domains and predicted topology (NP_001275936.1). Blue: transmembrane domains. Orange: extramembrane domains. Red: Location of patient mutations. *Top*: extracellular; *Bottom*: intracellular. (*D*) Mutated residues across vertebrate evolution showing conservation in all noted species. Red: mutant amino acid.

Table 1. Clinical features of eight patients from four families with PMG

	Family I		Family II		Family III		Family IV	
Family number/ Patient ID	II-1	II-2	II-1	II-2	II-1	II-3	II-1	II-2
Mutation	p.W317R	p.W317R	p.W317R	p.W317R	p.L85R	p.L85R	p.L85R	p.L85R
Gender	F	M	F	F	F	F	F	M
Origin	Egypt	Egypt	Egypt	Egypt	Egypt	Egypt	Egypt	Egypt
Consanguinity	+	+	+	+	+	+	+	+
Weight at birth (kg)	3	3.25	3	2.9	3	3.1	2.5	3
Length at birth (cm)	50	49	49	48.5	47.5	47	46	50
HC at birth (SD)	−0.5	−0.6	−0.5	−0.9	−1.5	−1.2	−1.2	−0.8
HC at last examination (SD)	−4.5	−3.8	−3.2	−3.0	−4.5	−3.5	−4.0	−3.3
Age at diagnosis (m or y)	3 y 2 m	1 y 7 m	2 y	7 m	4 y	1 y 5 m	9 m	10 m
Hypertonia	+	+	+	+	+	+	+	+
Intellectual disability	profound	profound	severe	moderate	severe	moderate	profound	severe
Autistic-like behavior	−	−	−	−	−	+	−	−
Death (if yes, age m or y)	−	−	−	−	−	−	1 y 4 m	−
Age at last examination (m or y)	6 y 8 m	5y	7 y 10 m	2 y 10 m	4 y 5 m	2 y 2 m	1 y 3 m	1 y
Gross motor (normal/delay/ absent)	Delayed (cannot sit)	Delayed (cannot sit)	Delayed (sit with support)	Delayed (sit with support)	Delayed (cannot sit)	Delayed (sit with support)	Delayed (cannot sit)	Delayed (cannot sit)
Fine motor (normal/delay/ absent)	Delayed (cannot hold objects or use hands)	Delayed (cannot hold objects or use hands)	Delayed (cannot hold objects or use hands)	Delayed (cannot hold objects and feel self)	Delayed (cannot hold objects and feel self)	Delayed (cannot hold objects and feed self)	Delayed (cannot hold objects or use hands)	Delayed (cannot hold objects or use hands)
Language (normal/delay/ absent)	Absent	Absent	Absent	Absent	Absent	Absent	Absent	Absent
Social (normal/delayed / absent)	Delayed (interacts with others and knows parents)	Delayed (interacts with others and knows parents)	Delayed (interacts with others and knows parents)	Delayed (interacts with others and knows parents)	Absent (does not interact or recognize family)	Absent (does not interact or recognize family)	Absent (does not interact or recognize family)	Absent (does not interact or recognize family)
Seizures								
Onset	3 m	2 y	4 m	4 m	3 m	5 m	5 m	4 m
Type	GTC	GTC	Severe myoclonic	Severe myoclonic	Severe myoclonic	Severe myoclonic	Myoclonic, tonic	Myoclonic, tonic
Frequency seizures per day	3/d	1/d	1/d	4/d	3/d	3/d	5-10/d	1/d
Therapy	Valproate, Levetiracetam, Clonazepam	Levetiracetam	Valproate, Levetiracetam, Topiramate	Valproate, Levetiracetam	Valproate, Levetiracetam	Valproate, Levetiracetam	Valproate, Levetiracetam, Clonazepam	Levetiracetam
Other systemic findings								
Ophthalmic	−	−	−	−	−	−	Megalocornea	Megalocornea
Cardiovascular	−	−	−	−	−	−	−	−
Respiratory	−	−	−	−	Recurrent chest infection	−	Recurrent chest infection	−

Table 1. Clinical features of eight patients from four families with PMG (Continued)

	Family I		Family II		Family III		Family IV	
Family number/ Patient ID	II-1	II-2	II-1	II-2	II-1	II-3	II-1	II-2
Musculoskeletal	Hypertonia	Hypertonia	Hypertonia	Mild Hypertonia	Spastic	Hypertonia	Spastic	Hypertonia
Genitourinary	–	–	–	–	–	–	–	Micropenis
Investigations								
CPK level (mg/dl)	96	140	125	98	58	90	80	112
Other metabolic findings	Normal	Normal	Normal	Normal	Normal	Normal	Normal	Normal
VEP/ERG	Normal	Normal	Normal	Normal	Normal	Normal	n/a	Normal
EMG	Normal	Normal	Normal	Normal	Normal	Normal	Normal	Normal
MRI								
Image diagnosis	Generalized PMG	Generalized PMG	Generalized PMG	Generalized PMG	Generalized PMG	Generalized PMG	Generalized PMG	Generalized PMG
Cobblestone lissencephaly	–	–	–	–	–	–	–	–
Hydrocephalus	–	–	–	–	–	–	–	–
Encephalocele	–	–	–	–	–	–	–	–
Dandy-Walker malformation	–	–	–	–	–	–	–	–
Corpus callosum defects	–	–	–	–	Thin corpus callosum	Thin corpus callosum	Thin corpus callosum	Thin corpus callosum
Brain stem anomalies	–	–	–	–	–	–	–	–
Cerebellar anomalies	Mild vermian hypoplasia	-	-	-	Mild vermian hypoplasia	Mild vermian hypoplasia	-	Mild vermian hypoplasia
Retrocerebellar cysts	+	–	–	–	-	+	–	–
Other	Dilated lateral ventricles	Dilated lateral ventricles	Dilated lateral ventricles	Dilated lateral ventricles	Dilated lateral ventricles	Dilated lateral ventricles	Dilated lateral ventricles	Dilated lateral ventricles

Legend: CPK: creatinine phosphokinase; EMG: electromyogram; ERG: electroretinogram; GTC: generalized tonic seizures; PMG: polymicrogyria; SD: standard deviation; VEP: visual evoked potentials.

laminar-like unit structures derived from rosettes. In patient BOs, these were seemingly randomly and diffusely distributed, while the overall number of CTIP2$^+$ cells was not statistically different. (Fig. 2 *L*–*O* and *SI Appendix*, Fig. S2*K*). These BO phenotypes suggest a defect in laminar-like unit structure formation.

The apical junction phenotypes suggested there may be defects in radial glial fiber integrity. We thus stained BOs at DIV52 with BLBP, a radial glial fiber lipid-binding protein, and SOX2 to label radial glial nuclei (22). Control BOs showed regularly spaced fibers oriented perpendicularly to the apical surface, whereas patient organoids showed scant discontinuous fibers with seemingly random orientation (Fig. 2 *P*–*S*). These findings suggest *TMEM161B* plays roles in establishing the radial glial scaffold.

***Tmem161b* Mutations Function as Hypomorphic Alleles In Vivo.** To understand the role of *TMEM161B* in vivo, we generated mouse models by knockin (KI) of both patient mutations and compared results with loss of function (LOF) alleles, using CRISPR-based gene editing to produce F0 (i.e., first-generation founder) "crispant" mice. An injection of 76 zygotes for each allele yielded mice homozygous for each patient mutation (L85R/L85R and W317R/W317R), biallelic LOF alleles (LOF/LOF) as well as compound heterozygous (L85R/LOF, W317R/LOF) (Fig. 3*A* and *SI Appendix*, Fig. S3*A*). A total of 24 mice were successfully edited to carry homozygous L85R, and 24 homozygous W317R with genotypes confirmed by Sanger sequencing (Fig. 3*B* and *SI Appendix*, Table S3). All F0 mice were harvested at embryonic day 18.5 (E18.5), and therefore survival, behavior, and transmission of mutations were not assessed.

Most striking was a craniofacial malformation in over half of LOF/LOF mice, with a "beaked" snout, microcephaly, jaw defects, and reduced retinal pigment (*SI Appendix*, Fig. S3*B* and Table S3). This phenotype most closely matches what has been called murine "otocephaly" complex, consisting of agnathia, eye defects, and holoprosencephaly (HPE) (23). Neither KI/KI, KI/LOF,+/KI nor +/LOF showed this phenotype, suggesting KI alleles are less severe than LOF. The other half of the LOF/LOF mice showed either completely absent cranium or normal appearance, possibly attributable to mosaicism or off-target CRISPR effects. However, there were no other gross malformations evident in the body or limbs, suggesting specificity of CRISPR targeting.

***Tmem161b* KI Mice Show Disorganized Radial Glial Fibers.** We noted no gross brain defects in any genotype except LOF/LOF, which showed the absence of the midline longitudinal fissure separating the two hemispheres in approximately 60% (11/18). This finding was consistent with partially penetrant HPE, also part

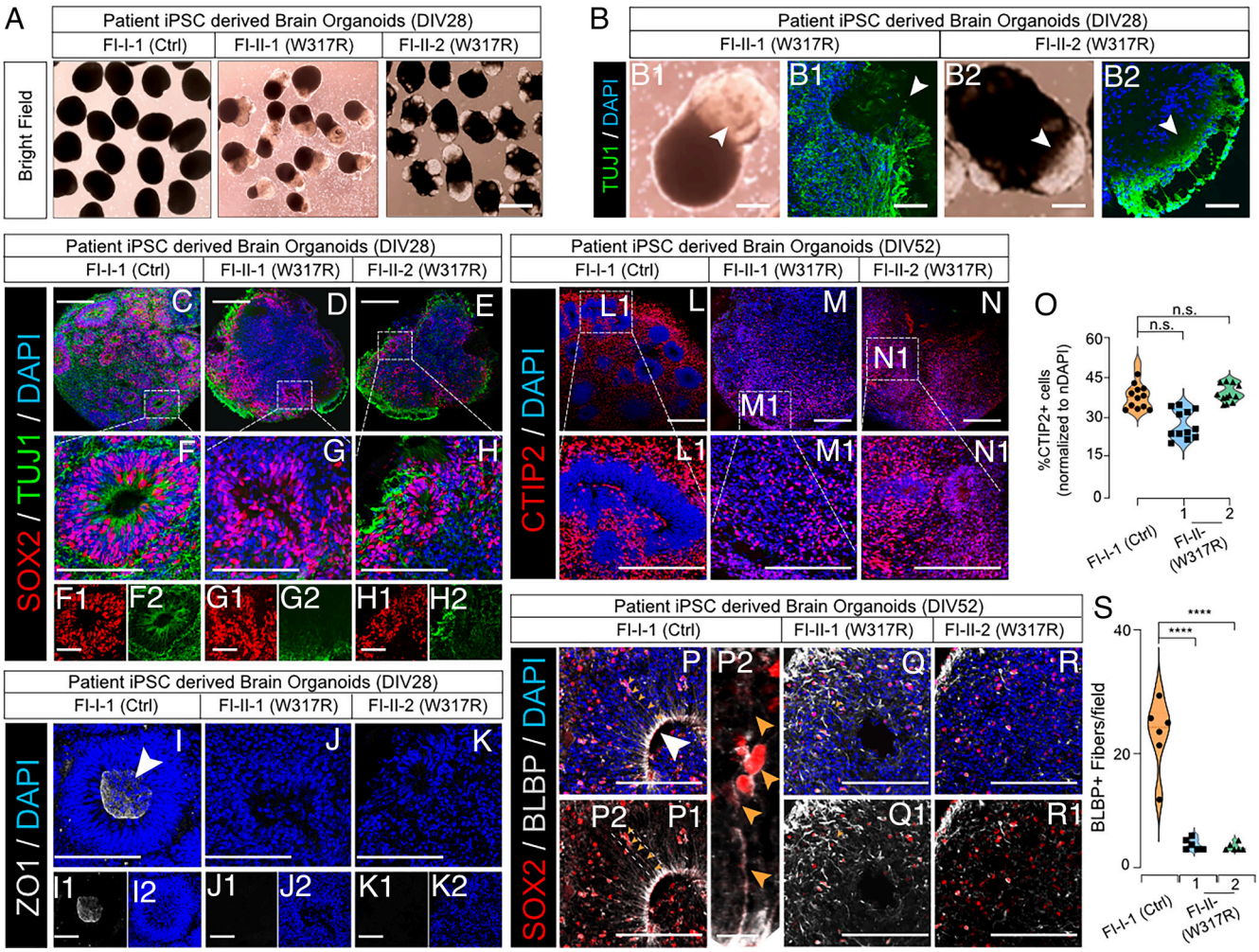

Fig. 2. Patient BOs show impaired apical junctions and glial scaffolding. (*A*) Patient BOs derived from FI-II-1 and FI-II-2 iPSCs carrying p.W317R show multiple bulbous cyst-like tags (arrows) compared to unaffected controls at days in vitro (DIV) 28. FI: Family I. (Scale bar: 1 mm.) (*B*) TUJ1 and DAPI stain of cyst-like structures from *A* at DIV28 show cell sparse region with occasional bridging TUJ1 fibers (B1 to B2). (Scale bar: 400 μm.) (*C–H*) Loss of neural rosettes organization in patient BOs at DIV28, stained for SOX2, TUJ1 and DAPI. FI-I-1(Ctrl) shows well-spaced rosettes (magenta) surrounded by TUJ1 immature neurons, whereas mutant shows disorganized rosette-like structures, with TUJ1 restricted to distal regions. (*F–H*) Zoom-in panels of single neural rosettes. Bar: 100 μm in F1-H1, F2-H2, 200 μm in *F–H*, and 400 μm in *C–E*. (*I–K*) Loss of apical junctions (AJs) in patient BOs at DIV28. FI-I-1 (Ctrl) shows spherical ZO-1$^+$ zone representing AJs, not apparent in patient BOs. Bar: 200 μm. (*L–N*) Loss of lamina-like structures in patients BOs at DIV52, stained for CTIP2 (deep layer marker) and DAPI. (L1-N1) Zoom-in panel of lamina-like structure single unit, derived from single rosette. Bar: 400 μm. (Zoom-in scale bar: 200 μm.) (*O*) Quantification of percent of CTIP2$^+$ cells per field. n.s. not significant, numbers of DAPI as reference; n = 12 includes three BOs from different biological replicates and 4 image regions from each section. Multiple *t* test followed by a Šidák multiple-comparison test correction measured significance. (*P–R*) Impaired BLBP$^+$ radial glial fibers in patient BOs at DIV52. FI-I-1 (Ctrl) shows AJs (arrowhead) emanating multiple radial fibers (orange arrowheads), whereas mutant shows AJs as well as disorganized BLBP$^+$ fibers. P1-R1: Single fluorescence channel showing disrupted BLBP staining. P2: SOX2$^+$ cell (red) apparently adhered to BLBP$^+$ radial glia. (Scale bar: 200 μm.) (*S*) Quantification of BLBP$^+$ fibers per field. n = 12 includes three BOs from different biological replicates and four image regions from each section. Multiple *t* test followed by a Šidák multiple-comparison test correction determined significance. ****$P < 0.0001$.

of the otocephaly phenotype (Fig. 3*C* and *SI Appendix*, Table S3) (23, 24). KI/KI showed a similar appearance to wildtype, again suggesting missense alleles are hypomorphic.

We next performed SATB2 immunostaining to label upper-layer neurons across the allelic series. WT mice showed SATB2 expression restricted to upper layers as expected (Fig. 3*D*) (25). For both patient variants, we found SATB2$^+$ cells were partially mispositioned to progenitor layers in the KI/KI conditions (i.e., bin 5 to 6) (Fig. 3 *E–G*), with similar phenotypes observed in the KI/LOF conditions (*SI Appendix*, Fig. S4 *A* and *B*). In LOF/LOF, we observed a thinner cortex with mispositioned SATB2$^+$ cells across most layers excluding layer I (*SI Appendix*, Fig. S4 *C* and *D*).

To test for defective radial glia scaffold seen in BOs, we again stained for BLBP. For both variants in KI/KI conditions, we found brains showed discontinuous BLBP fibers spanning from apical surface to pia, indicating a role for *Tmem161B* in radial glial fiber integrity (Fig. 3 *H–J* and *SI Appendix*, Fig. S4 *E–H*) (26).

TMEM161B Mediates Actin Filopodia (AF) through Rho-GTPase CDC42. From the BioGrid protein interaction database, we found TMEM161B is predicted to interact with several actin-regulators and G-protein coupled receptors functioning in cytoskeletal pathways (*SI Appendix*, Fig. S5*A* and Table S5) (27). To assess potential roles in cytoskeletal function, we expressed Flag-tagged TMEM161B in heterologous cells. Transfected cells showed TMEM161B tagged protein localized predominantly to the cell membrane. Additionally, transfected cells showed prominent spikes protruding radially from the cell membrane (Fig. 4 *A* and *B*), reminiscent of AF. We thus co-stained with phalloidin to label F-actin and found apposed co-localization (Fig. 4*B*). These results were confirmed by forced expression in wildtype human neural precursor cells (hNPCs) (*SI Appendix*, Fig. S5 *B–E*). These results suggest TMEM161B localizes to the cell membrane to regulate AF formation.

To assess whether TMEM161B variants influence the AF phenotypes, we introduced these mutations by site-directed mutagenesis

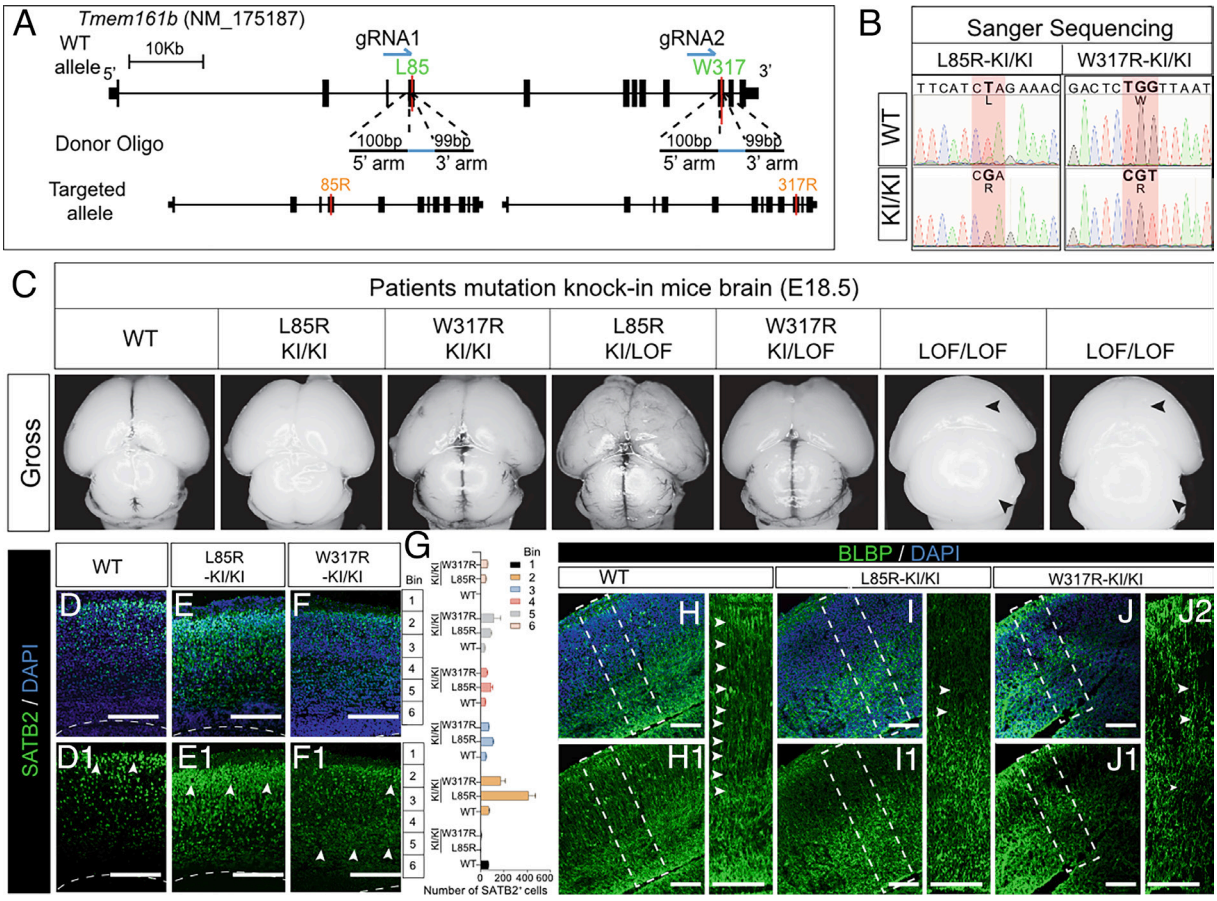

Fig. 3. *Tmem161b* patients mutation crispant KI mice show disrupted radial glial scaffolding. (*A*) Generation of patient mutations knock-in mice. Guide and donor oligos targeting exon 4 and 10, respectively (red) to introduce L85R and W317R alleles utilizing non-homologous end joining (NHEJ). In addition, NHEJ generated null loss-of-function (LOF) alleles (See *SI Appendix*, Fig. S3 for details). (*B*) Sanger sequencing chromatograms of tail genotypes showing homozygous KI L85R and W317R variants. (*C*) CRISPR-F0 (first generation) LOF/LOF mice show fusion of the cerebral hemispheres and cerebellar hemispheres (far *Right*, arrows), consistent with holoprosencephaly. No differences were noted between WT and any of the homozygous KI or compound heterozygous KI at the gross level. Black: residual pial hemosiderin from dissection. (*D–F*) Disorganized cortical lamination in KI/KI mice brain compared to WT. SATB2 mostly marks upper layer neurons at E18.5 in WT. Homozygous KI mutants show downward displacement of SATB2$^+$ cells. There was also an increase in number of SATB2$^+$ labeled cells counted in Bin 4 to 6 per field. DAPI: nuclei. Bar: 400 μm. (*G*) Quantification of laminar position SATB2$^+$ labeled cells. n = 3 mice per genotype from eight sections. Representative images shown. (*H–J*) BLBP immunostaining show impaired radial glial fiber organization in KI/KI mice compared to WT. CRISPR-F0 mice brain immunostained for BLBP across WT in *H*, L85R-KI/KI in *I*, W317R-KI/KI in *J*. Split panels show BLBP staining in H1 for WT, I1 for L85R-KI/KI, and J1 for W317R-KI/KI. Zoom in panel shows BLBP staining and schematic in H2 for WT. I2 for L85R-KI/KI. J2 for W317R-KI/KI. Arrows in *D–F*: SATB2$^+$ cells enriched layers. Arrows in *H–J*: radial fibers. DAPI: nuclei. (Scale bar: 400 μm.)

into the full-length cDNA, then compared phenotypes. As expected, patient mutations showed a statistically significant abrogation in AF formation, suggesting impaired TMEM161B-induced AF (Fig. 4 *C–E* and *SI Appendix*, Fig. S5*F*).

We next assessed mechanisms by which TMEM161B might regulate AF. BioGrid analysis suggested potential interaction with several CDC42 effectors, including ZO-1, encoded by *TJP1* (*SI Appendix*, Fig. S5*G*). ZO-1 is essential for the development of apical junctions in vivo and in vitro, recruiting CDC42 effector kinases to modulate actin protrusions (28). We thus assessed the role of CDC42 in TMEM161B-induced AF. Co-expression of a constitutively active form of CDC42 (Q61L) showed no significant effect on TMEM161B-induced AF. However, a dominant negative form of CDC42 (T17N), incapable of exchanging GTP for GDP, significantly abrogated the TMEM161B-induced AF (Fig. 4 *F–H* and *SI Appendix*, Fig. S5 *H–I*) (29). Moreover, the loss of AF caused by TMEM161B patient mutations was partially rescued by co-expression of a constitutively active form CDC42 (Q61L) (*SI Appendix*, Fig. S5 *J–L*). We conclude that TMEM161B likely mediates AF through the regulation of CDC42 function.

Discussion

Gyrification mechanisms have been debated for decades, and there is still not a generally accepted model for this process during brain development. Our study identifies TMEM161B in gyral spacing in humans, likely impacting radial glial cell polarity through effects on the actin cytoskeleton. In our prior studies involving 33,748 UK Biobank participants that underwent structural brain MRI and genome-wide SNP genotyping, we associated *TMEM161B* (among other variants) with neocortical sulcal depth ($P = 9.56 \times 10^{-14}$) and cortical surface area ($P = 1.28 \times 10^{-7}$) (30). Whether the effect of these SNPs is on *TMEM161B* expression will require further work, but this suggests a role for *TMEM161B* in cortical gyrification both in healthy and diseased states.

We found TMEM161B forced expression leads to abundant actin filopodial cell protrusions, likely functioning upstream of CDC42, a critical factor involved in cell polarity (31). Taken together with the observed defects in apical junctions, the data suggests TMEM161B may modulate actin in radial glial progenitors. Prior work established critical roles for CDC42 in RGCs. Conditional deletion of *Cdc42* in RGCs leads to the gradual

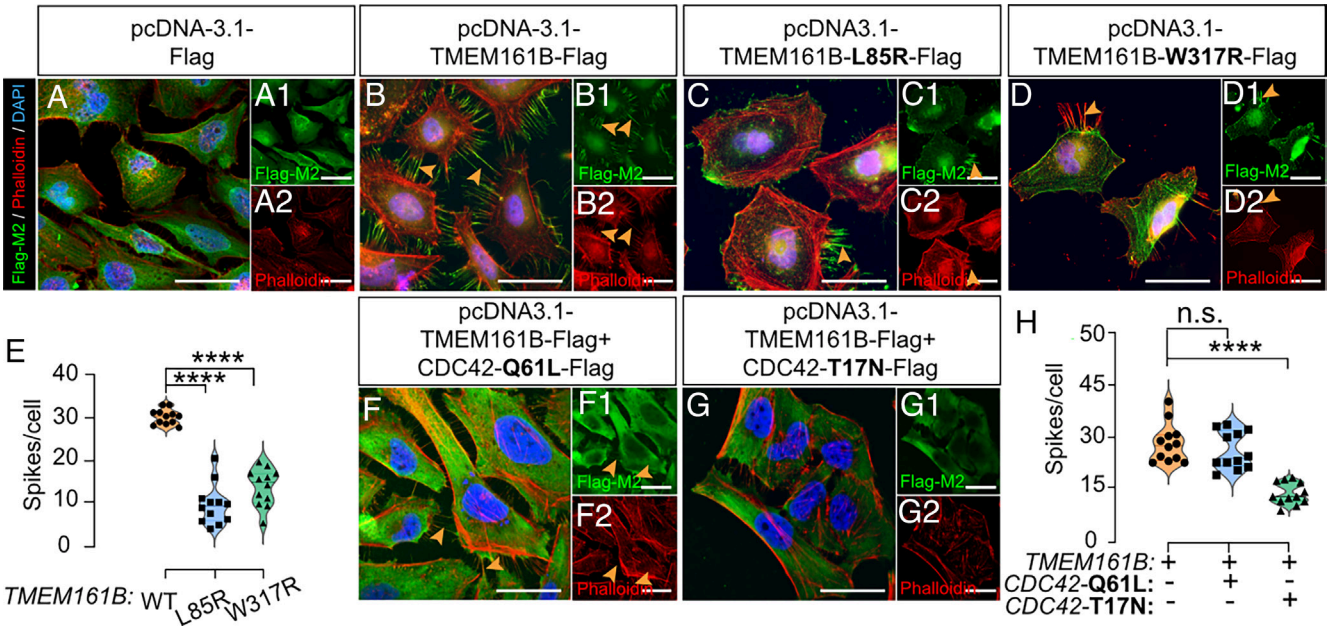

Fig. 4. *TMEM161B* modulates AF formation through Rho GTPase CDC42. (*A* and *B*) Forced expression of Flag-tagged TMEM161B (green) leads to filopodia formation in Hela cells. Co-staining with Phalloidin documents these as AF. Single channel image shows Flag-M2 staining in A1 and B1, Phalloidin staining in A2 and B2. DAPI: nuclei; (Scale bar: 20 μm.) (*C* and *D*) Forced expression of patient missense mutations shows abrogated AF phenotype compared with WT TMEM161B. *C*: L85R, *D*: W317R Flag-M2 stained (green) with Phalloidin (red). Single-channel image shows Flag-M2 staining in C1 and D1, Phalloidin staining in C2 and D2. DAPI: nuclei; (Scale bar: 20 μm); Orange arrows: actin spikes. (*E*) Patient mutations show abrogated AF phenotype compared with WT. Quantification of AF per cell shown in *B*–*D*. n = 12 includes three different biological replicates and four image regions from each section; Multiple t test followed by a Šidák multiple-comparison test correction determined significance. $^{**}P < 0.01$. (*F* and *G*) Dominant negative CDC42 abrogates AF induced by TMEM161B forced expression, whereas constitutively active CDC42 shows no impact on TMEM161B AF phenotype. Immunostaining of Hela cell cultures co-force expressed with TMEM161B-Flag with CDC42-Q61L or CDC42-T17N against anti-Flag-M2 and Phalloidin. Single-channel image shows Flag-M2 staining in F1, Phalloidin staining in F2. DAPI: nuclei; (Scale bar: 20 μm); Orange arrows: AF. (*H*) Quantification of AF shown in *B*, *F*, and *G*. n = 12 includes three different biological replicates and four image regions from each section; multiple *t* test followed by a Šidák multiple-comparison test correction determined significance. $^{**}P < 0.01$.

disappearance of adherens junctions that impairs the formation of radial fibers (11, 12). This is thought to be mediated in part through interactions with MARCKS and GSK3 (32, 33). The apical junction is also the site of ciliary protrusion in polarized epithelia, and in the accompanying paper, Akula et al. (34) observed disruption of apical primary cilia in *Tmem161b* KO mice, in line with a role in RGC polarity (35).

TMEM161B protein family first appeared evolutionarily in sponges, which lack a nervous system entirely, and together with its highly conserved sequence, suggests evolutionarily conserved functions. Thus, we think TMEM161B is less likely to play a direct role in gyrification, but rather in cell polarity in metazoan complex tissues like brain. Although we could not exclude non-cell autonomous functions, forced expression leads to cell-autonomous effects on actin, consistent with the cell autonomous roles proposed by Akula et al. in the accompanying paper from in utero electroporation studies.

Tmem161b mouse knockouts showed partially penetrant HPE and otocephaly, unexpected findings given that none of our patients showed midline defects. HPE is thought to reflect requirements for Sonic hedge (Shh) and TGF-b signaling at the brain midline (36, 37). One potential mechanism may be through Cdc42, which has been implicated in a Shh independent form of HPE (12). Thus, our data implicating TMEM161B in murine HPE may suggest shared mechanisms between the formation of the brain midline and cortical gyrification.

Materials and Methods

Materials. The raw exome sequencing files for the four families are available at dbGaP accession phs000382.v3.p1, and mutations available at Matchmaker Exchange. Human iPSC lines used in the current study were obtained from CIRM (CIRM-IT1-06611). All iPSC lines reprogrammed at Cellular Dynamics, Inc (Madison, WI) and passed QCs for chromosomal integrity (by SNP microarray), pluripotency (by analysis of gene expression by qPCR of 48 mRNAs) and identity confirmation (by genotyping) and tested negative monthly for mycoplasma. All mice were generated at the Jackson Laboratory Genetic Engineering Technology service under the standard animal protocols. MRI GWAS analyses made use of the data from participants of the UK Biobank population cohort, obtained from the data repository under accession number 27412. The details of this analysis and statistical tests are described elsewhere (30). Further information and requests for resources and reagents should be directed to and will be fulfilled by the Lead Contact, Dr. Joseph Gleeson (jogleeson@ucsd.edu).

Human Subjects. This study was reviewed and approved by the University of California San Diego Institutional Review Board operates under Federalwide Assurance number, FWA00004495, with protocol IRB 171094X entitled "Generating human neuronal models of childhood neurological disorders." All participants and/or their parents/guardians provided written informed consent to participate in this study.

Cell Culture. HEK293T cells (sex typed as female) and Hela cells (sex typed as female) were obtained from ATCC (CRL-11268™) and ATCC (CCL-2™) were not further authenticated. Human pluripotent stem cells were from CIRM (CIRM-IT1-06611). Patients fibroblast cells were derived from patient skin punches under approved IRB (171094X). Human neural progenitor cells (hNPCs) were generated from healthy hiPSCs. All cells tested negative for mycoplasma monthly. hBOs were generated as previously described (19).

Immunostaining. BOs, Hela and hNPCs fixed, cryosection, and stained as previously described (19). Overfixed E18.5 mice brains were cryosectioned and stained as previously described (38). Images were taken with ZEISS LSM880 Airyscan, with post-acquisition analysis in ImageJ-6.

Crispant Mice Generation. Candidate guide RNA sequences were selected using software from Benchling, Inc. (www.benchling.com). All RNA sequences

were obtained from Integrated DNA Technologies (IDT). crRNAs were annealed with trRNA following IDT Alt-R System protocols. All mouse procedures were conducted according to national and international guidelines (AALAC and IACUC) and have been approved by JAX Animal Care and Use Committee.

Genomic DNA was extracted from embryonic tail tips and editing sites of the *Tmem161b* genomic loci were PCR amplified using primers listed in *SI Appendix*, Table S4. PCR products were analyzed by Sanger sequencing. The Inference of CRISPR Editing deconvolution tool from Synthego (2019. V2.0.) was used.

Transfection, Western Blot, and Cloning. The transfection, western blot, and cloning were performed with standard protocols (19). For transfection, Lipofectamine™3000 was used according to the manufacturer's protocol. The primers to generate clones are listed in *SI Appendix*, Table S4.

Quantification and Statistical Analysis. Statistical analysis was performed with the GraphPad Prism 9 software. We compared differences in relative mRNA expression level, cell numbers by two-way ANOVA followed by a Šidák multiple-comparison test. In all statistics, n = 12 includes three from different biological replicates and four technical replicates. Multiple *t* tests followed by a Šidák multiple-comparison test correction were used to determine significance. ****$P < 0.0001$. Raw quantification data is available in *SI Appendix*, Table S6.

Data, Materials, and Software Availability. Raw exome sequencing files data have been deposited in dbGaP (phs000382.v3.p1). All study data are included in the article and/or *SI Appendix*.

ACKNOWLEDGMENTS. L.W. received support from NIH/NINDS Pathway to independent K99/R00 award (1K99NS125106-01A1), CIRM Training Grant Postdoc award (EDUC4-12804) and the BBRF (grant 28771). Y.-J.H received funding from Ministry of Health & Welfare, Republic of Korea (HI19C1330). We acknowledge Drs. Trey Ideker, Sangwoo Kim, and members of the Gleeson Lab for feedback, Gene Matcher for connecting us with Drs. Shyam Akula and Christopher A. Walsh and Dr. Kelly Smith for communicating preliminary data. This work was supported by the Rady Children's Hospital Neuroscience Endowment and the HHMI to J.G.G., the UCSD Microscopy Core (NINDS grant P30NS047101), CCBB supported by NIH grant UL1TR001442, CIRM grant IT1-06611 for generation of IPCSs, the Yale, GMKF and NIH X01HG011360 to support genotyping at CIDR, NIH X01HD100698 to support genome sequencing, Broad Institute Center for Mendelian Genomics NIH grant UM1HG008900, and OD030187 to C.H. and S.A.M. for generation of mice models, the generation of CRISPR/Cas9 edited embryos was supported in part by the Genetic Engineering Technology core and Cancer Center Support grant (CA034196), O.A.A. obtained support from the Research Council of Norway (#223273).

Author affiliations: [a]Department of Neurosciences, University of California San Diego, La Jolla, CA 92093; [b]Rady Children's Institute for Genomic Medicine, Rady Children's Hospital, San Diego, CA 92123; [c]The Jackson Laboratory, Bar Harbor, ME, 04609; [d]Department of Biomedical Systems Informatics, Yonsei University, Seoul 03722, S. Korea; [e]Department of Developmental and Cell Biology, University of California Irvine, Irvine, CA 92697; [f]Norwegian Centre for Mental Disorders Research, Division of Mental Health and Addiction, Oslo University Hospital and Institute of Clinical Medicine, University of Oslo, Oslo 0424, Norway; [g]The Department of Cognitive Science, University of California San Diego, La Jolla, CA 92093; [h]Clinical Genetics Department, Human Genetics and Genome Research Institute, National Research Centre, Cairo 12311, Egypt; and [i]Department of Pediatrics, Division of Genetics and Metabolism, University of Minnesota, Minneapolis, MN 55455

1. R. Stahl *et al.*, Trnp1 regulates expansion and folding of the mammalian cerebral cortex by control of radial glial fate. *Cell* **153**, 535–549 (2013).
2. L. F. Franchini, Genetic mechanisms underlying cortical evolution in mammals. *Front Cell Dev. Biol.* **9**, 591017 (2021).
3. P. Pillay, P. R. Manger, Order-specific quantitative patterns of cortical gyrification. *Eur J. Neurosci.* **25**, 2705–2712 (2007).
4. A. R. Judkins, D. Martinez, P. Ferreira, W. B. Dobyns, J. A. Golden, Polymicrogyria includes fusion of the molecular layer and decreased neuronal populations but normal cortical laminar organization. *J. Neuropathol. Exp. Neurol.* **70**, 438–443 (2011).
5. A. C. Jansen *et al.*, The histopathology of polymicrogyria: A series of 71 brain autopsy studies. *Dev. Med. Child Neurol.* **58**, 39–48 (2016).
6. C. A. Stutterd, W. B. Dobyns, A. Jansen, G. Mirzaa, R. J. Leventer "Polymicrogyria overview" in *GeneReviews((R))*, M. P. Adam *et al.*, Eds. (University of Washington, Seattle, WA, 2018), updated.
7. K. Campbell, M. Gotz, Radial glia: Multi-purpose cells for vertebrate brain development. *Trends Neurosci.* **25**, 235–238 (2002).
8. P. Rakic, "389Radial glial cells: Scaffolding for cortical development and Evolution" in *Neuroglia*, H. Kettenmann, B. R. Ransom, Eds. (Oxford University Press, 2004). 10.1093/acprof:oso/9780195152227.003.0031.
9. T. J. Nowakowski, A. A. Pollen, C. Sandoval-Espinosa, A. R. Kriegstein, Transformation of the radial glia scaffold demarcates two stages of human cerebral cortex development. *Neuron* **91**, 1219–1227 (2016).
10. H. Jinnou *et al.*, Radial glial fibers promote neuronal migration and functional recovery after neonatal brain injury. *Cell Stem. Cell* **22**, 128–137.e129 (2018).
11. S. Cappello *et al.*, The Rho-GTPase cdc42 regulates neural progenitor fate at the apical surface. *Nat Neurosci* **9**, 1099–1107 (2006).
12. L. Chen *et al.*, Cdc42 deficiency causes Sonic hedgehog-independent holoprosencephaly. *Proc. Natl. Acad. Sci. U.S.A.* **103**, 16520–16525 (2006).
13. X. Ma *et al.*, A novel regulator of ER Ca(2+) drives Hippo-mediated tumorigenesis*Oncogene* **39**, 1378–1387 (2020).
14. C. D. Koopman *et al.*, The zebrafish grime mutant uncovers an evolutionarily conserved role for Tmem161b in the control of cardiac rhythm. *Proc. Natl. Acad. Sci. U.S.A.* **118**, e2018220118 (2021).
15. J. Jumper *et al.*, Highly accurate protein structure prediction with AlphaFold. *Nature* **596**, 583–589 (2021).
16. R. Steinhaus *et al.*, MutationTaster2021. *Nucleic. Acids Res.* **49**, W446–W451 (2021).
17. T. J. Nowakowski *et al.*, Spatiotemporal gene expression trajectories reveal developmental hierarchies of the human cortex. *Science* **358**, 1318–1323 (2017).
18. T. Kadoshima *et al.*, Self-organization of axial polarity, inside-out layer pattern, and species-specific progenitor dynamics in human ES cell-derived neocortex. *Proc. Natl. Acad. Sci. U.S.A.* **110**, 20284–20289 (2013).
19. L. Wang *et al.*, Loss of NARS1 impairs progenitor proliferation in cortical brain organoids and leads to microcephaly. *Nat. Commun.* **11**, 4038 (2020).
20. A. M. Pasca *et al.*, Functional cortical neurons and astrocytes from human pluripotent stem cells in 3D culture. *Nat. Methods* **12**, 671–678 (2015).
21. P. Arlotta *et al.*, Neuronal subtype-specific genes that control corticospinal motor neuron development in vivo. *Neuron* **45**, 207–221 (2005).
22. L. Feng, M. E. Hatten, N. Heintz, Brain lipid-binding protein (BLBP): A novel signaling system in the developing mammalian CNS. *Neuron* **12**, 895–908 (1994).
23. I. Matsuo, S. Kuratani, C. Kimura, N. Takeda, S. Aizawa, Mouse Otx2 functions in the formation and patterning of rostral head. *Genes. Dev.* **9**, 2646–2658 (1995).
24. K. A. Schachter, R. S. Krauss, Murine models of holoprosencephaly. *Curr. Top. Dev. Biol.* **84**, 139–170 (2008).
25. O. Britanova *et al.*, Satb2 is a postmitotic determinant for upper-layer neuron specification in the neocortex. *Neuron* **57**, 378–392 (2008).
26. D. Del Toro *et al.*, Regulation of cerebral cortex folding by controlling neuronal migration via FLRT adhesion molecules. *Cell* **169**, 621–635.e616 (2017).
27. E. L. Huttlin *et al.*, Dual proteome-scale networks reveal cell-specific remodeling of the human interactome. *Cell* **184**, 3022–3040.e3028 (2021).
28. M. A. Odenwald *et al.*, The scaffolding protein ZO-1 coordinates actomyosin and epithelial apical specializations in vitro and in vivo. *J. Biol. Chem.* **293**, 17317–17335 (2018).
29. P. Nalbant, L. Hodgson, V. Kraynov, A. Toutchkine, K. M. Hahn, Activation of endogenous Cdc42 visualized in living cells. *Science* **305**, 1615–1619 (2004).
30. D. van der Meer *et al.*, The genetic architecture of human cortical folding. *Sci. Adv.* **7**, eabj9446 (2021).
31. D. I. Johnson, Cdc42: An essential Rho-type GTPase controlling eukaryotic cell polarity. *Microbiol. Mol. Biol. Rev.* **63**, 54–105 (1999).
32. J. M. Weimer *et al.*, MARCKS modulates radial progenitor placement, proliferation and organization in the developing cerebral cortex. *Development* **136**, 2965–2975 (2009).
33. Y. Yokota *et al.*, Cdc42 and Gsk3 modulate the dynamics of radial glial growth, inter-radial glial interactions and polarity in the developing cerebral cortex. *Development* **137**, 4101–4110 (2010).
34. S. K. Akula *et al.*, TMEM161B regulates cerebral cortical gyration, Sonic Hedgehog signaling, and ciliary structure in the developing central nervous system. *Proc. Natl. Acad. Sci. U.S.A* **120**, e2209964120 (2023).
35. H. Higginbotham *et al.*, Arl13b-regulated cilia activities are essential for polarized radial glial scaffold formation. *Nat. Neurosci.* **16**, 1000–1007 (2013).
36. T. Maity, N. Fuse, P. A. Beachy, Molecular mechanisms of Sonic hedgehog mutant effects in holoprosencephaly. *Proc. Natl. Acad. Sci. U.S.A.* **102**, 17026–17031 (2005).
37. J. Massague, S. W. Blain, R. S. Lo, TGFbeta signaling in growth control, cancer, and heritable disorders. *Cell* **103**, 295–309 (2000).
38. G. Chai *et al.*, Mutations in spliceosomal genes PPIL1 and PRP17 cause neurodegenerative pontocerebellar hypoplasia with microcephaly. *Neuron* **109**, 241–256.e249 (2021).